Biogeosciences Discussions

Biogeosciences Discussions is the access reviewed discussion forum of *Biogeosciences*

The consumption of atmospheric methane by soil in a simulated future climate

C. L. Curry

Canadian Centre for Climate Modelling and Analysis, Climate Research Division, Environment Canada, Victoria, B.C., Canada

Correspondence to: C. L. Curry (charles.curry@ec.gc.ca)

BGD

6, 6077–6110, 2009

Future consumption of methane by soil

C. L. Curry

Full Screen / Esc

Printer-friendly Version

Interactive Discussion

C. L. Curry

Full Screen / Esc

Printer-friendly Version

Interactive Discussion

Abstract

A recently developed model for the consumption of atmospheric methane by soil (Curry, 2007) is used to investigate the global magnitude and distribution of methane uptake in a simulated future climate. In addition to solving the one-dimensional diffusion-reaction equation, the model includes a parameterization of biological CH_4 oxidation that is sensitive to soil temperature and moisture content, along with simple scalings for land cultivation and wetland fractional coverage. Under the SRES emission scenario A1B, the model projects an 8% increase in the global annual mean CH_4 soil sink by 2100, over and above the 15% increase expected from increased CH_4 concentration alone. While the largest absolute increases occur in cool temperate and subtropical forest ecosystems, the largest relative increases in consumption (>40%) are seen in the boreal forest, tundra and polar desert environments of the high northern latitudes. Methane uptake at mid- to high northern latitudes increases year-round in 2100, with a 68% increase over present-day values in June. This increase is primarily due to enhanced soil diffusivity resulting from increased evaporation and reduced snow cover. At lower latitudes, uptake is enhanced mainly by elevated soil temperatures and/or reduced soil moisture stress, with the dominant influence determined by the local climate.

1 Introduction

Significant changes in the atmospheric concentrations of long-lived greenhouse gases (GHGs) have accompanied large-scale climate change over the Holocene, including the global warming of recent decades. The influence of climate change on the budgets of the same GHGs is thus a topic of great interest, and one that is beginning to be addressed by models of biogeochemical cycles at the global scale (Denman et al., 2007). The topic of this paper is the uptake of methane by soils, a process that represents a small but important sink of atmospheric CH_4 at the global scale, accounting for approx-

Future consumption of methane by soil

C. L. Curry

Printer-friendly Version

Interactive Discussion

imately 5% of the total. According to a recent meta-analysis of 318 annual estimates of uptake in wide range of ecosystems (Dutaur and Verchot, 2007), the total annual CH_4 uptake ranges from 12–59 Tg CH_4 yr^{-1}, with a narrower estimate of 22±12 Tg CH_4 yr^{-1} if the measurements are stratified by climatic zone, ecosystem, and soil texture.

5   Uptake of methane in soil occurs via oxidation by aerobic bacteria, or methanotrophs, several varieties of which have now been identified (Hanson and Hanson, 1996), but the precise mechanisms of which are still not well understood (Roslev et al., 1997; Knief et al., 2003; Horz et al., 2005). In a previous paper (Curry, 2007) (hereafter Paper I), a physical parameterization of this process was introduced, building on the

10   prior work of Ridgwell et al. (1999) (hereafter R99). In this scheme, the controlling variables of the uptake, deduced from numerous empirical studies – namely, the diffusion coefficient D_{soil} and the rate of biological oxidation k – were each expressed as the product of several factors sensitive to local, time-dependent, environmental conditions. Free parameters of the scheme were calibrated using multi-year field measurements,

15   and offline simulations conducted using observed (reanalysis) surface climatology. The simulated magnitude (28.0 Tg CH_4 a^{-1} in the global and annual mean) and seasonality of CH_4 uptake were shown to behave in a reasonable manner at several sites with widely varying climate and soil texture.

In the present paper, the same uptake scheme is driven not with reanalysis data,
20   as in Paper I, but rather with the simulated surface climate of an atmospheric general circulation model (GCM) coupled to a slab ocean. This configuration permits time-slice simulations of not just the present day methane uptake pattern, but also its past and future geographical distributions. The subsurface temperature increases associated with atmospheric warming are generally expected to enhance methanotropic activity,
25   except where reduced soil water availability leads to moisture stress. Simulations of uptake coupled to climate are therefore required to address uncertainty in the competing influences of increased soil diffusivity and reduced soil water availability over much of the tropical and mid-latitude land area in a warmer world. Field studies have shown that consumption may either increase or decrease depending upon moisture

availability and clade-specific biology (Schnell and King, 1996; Torn and Harte, 1996; Horz et al., 2005).

In the following section, I review the parameterization of methane uptake, and in Sect. 3 describe how it is applied in a coupled GCM in order to simulate CH_4 consumption under arbitrary atmospheric forcing. Simulated methane uptake in the present climate is then discussed in Sect. 4, while Sect. 5 contains results for simulated future (and preindustrial) climates. In the final section, I compare the results obtained here with those predicted from simpler soil methane consumption schemes, and conclude the paper with some remarks on directions for future progress.

2   Model overview

In this section I provide a brief review of the methane uptake scheme, the details of which may be found in Paper I. Soil methane uptake at the surface, J, is obtained from the first integral of the one-dimensional diffusion-reaction equation, which after some manipulation takes the simple form

$$J = g_0 \, C_{CH_4} \, r_C \, r_W \, (D_{soil} \, k_0 \, r_T \, r_{SM})^{1/2}, \tag{1}$$

where

J: surface flux (uptake) ($mg \, CH_4 \, m^{-2} d^{-1}$);
g_0=586.7 $mg \, CH_4 \, ppmv^{-1} \, s \, d^{-1} \, m^{-2} \, cm^{-1}$, conversion factor from mixing ratio to concentration;
C_{CH_4}: CH_4 mixing ratio at the surface (ppmv);
k_0: first-order oxidation rate constant, =$5.0 \times 10^{-5} \, s^{-1}$, determined from calibration with field data (Paper I);
r_C, r_W: dimensionless factors (0–1.0) for inhibition of uptake in cultivated soils and wetland areas, respectively (spatial maps are available as online auxiliary material of Paper I);

|◄   ►|

◄   ►

Back   Close

Full Screen / Esc

Printer-friendly Version

Interactive Discussion

r_T: dimensionless soil temperature factor (0–4.1), increasing for $-10 \leq T_{\text{soil}} \leq 27.5°C$, and decreasing for $T_{\text{soil}} > 27.5°C$;

r_{SM}: dimensionless factor (0–1.0) for inhibition of uptake due to sub-optimal soil moisture. r_{SM} is assumed to be optimal (= 1) for soil water potential $\psi < 0.2$ MPa, and to decrease smoothly to zero as ψ increases to 100 MPa, above which $r_{\text{SM}} = 0$. The exact forms of r_T and r_{SM} may be found in Paper I.

The diffusion coefficient in soil, D_{soil}, is given by

$$D_{\text{soil}} = 0.196 \, (1.0 + 0.0055 \, T_{\text{soil}}) \, \Phi^{4/3} \left(\frac{\Phi_{\text{air}}}{\Phi} \right)^{1.5 + 3/b} \text{cm}^2 \, \text{s}^{-1}, \tag{2}$$

where

Φ: total porosity ($\text{cm}^3 \, \text{cm}^{-3}$),
Φ_{air}: air-filled porosity ($\text{cm}^3 \, \text{cm}^{-3}$) $= \Phi - \theta$,
$\theta = \theta_w + \theta_i$,
θ_w: fractional water content,
θ_i: fractional ice content,
$b = 15.9 f_{\text{clay}} + 2.91$, f_{clay}: fraction of clay.
All quantities are taken to be two-dimensional fields, averaged over the top soil layer depth (10 cm). The dependence of J on the square root of D_{soil} and $k \equiv k_0 \, r_T \, r_{\text{SM}}$, as opposed to the linear dependence assumed by R99 and others, has recently received support from field and laboratory studies (von Fischer et al., 2009).

3   Methodology and simulations

The methane consumption algorithm was incorporated into the Canadian Centre for Climate Modelling and Analysis (CCCma) third generation atmospheric GCM (AGCM3), an improved version of the model described in McFarlane et al. (1992). AGCM3 represents the horizontal structure of the main prognostic variables using a

Future consumption of methane by soil

C. L. Curry

spectral representation, with T63 truncation in the present application and a corresponding gaussian physics grid of $2.8° \times 2.8°$. There are 31 sigma-hybrid vertical levels between 995 mb and 1 mb. A further description of this model version may be found in Scinocca et al. (2009).

For the present application, the CH_4 uptake subroutine was included in CLASS (Canadian LAnd Surface Scheme) v2.7, the land scheme currently used in AGCM3 (Verseghy, 1991, 1996), which runs at a 15-min time step. The uptake calculation is applied only in the top (0–10 cm) soil layer of CLASS, below which measured oxidation rates are usually small. Within this layer, D_{soil} and k are assumed to be vertically homogeneous, although they do vary in the horizontal (i.e., from one grid cell to the next).

To enable the simulation of future climate, AGCM3 was coupled to a 50m-thick slab ocean model including a prognostic sea ice component. Specified surface flux ("q-flux") adjustments, derived from a prior model run in which SSTs are restored toward climatological values, were added to the slab model's temperature tendency equation at each time step in order to give a more realistic distribution of SSTs. This strategy suits the present application since it allows an evaluation of the CH_4 sink strength at all land points in a significantly altered climate at a reasonable computational cost.

The coupled atmosphere-slab ocean-sea ice system was forced with spatially and temporally uniform GHG concentrations which differ in the present and future eras. I discuss in detail below the results of two simulations: (1) a 40-year equilibrium run at present-day (circa 1994) GHG concentrations, and (2) a 40-year equilibrium run using GHG concentrations from the SRES A1B (ISAM reference) scenario at 2100, with CFC concentrations from the WMO98 Scenario A1. The simulations were started from the end states of previously archived runs at CCCma for $1 \times CO_2$ and $2 \times CO_2$ equilibrium climates. All other features of the model, in particular, the land cover including the cultivated fraction of each grid cell, were held fixed at their present-day distributions. As in Paper I, areas of permanent water, ice (e.g., Antarctica and all but a few grid cells over Greenland), and desert were masked out of the methane consumption calculation.

Future consumption of methane by soil

C. L. Curry

|◄ | ►|

◄ | ►

Back | Close

Full Screen / Esc

Printer-friendly Version

Interactive Discussion

After an adjustment period of 5–10 years after the start of each simulation (caused by the slight change in GHG concentrations), the global average top layer soil temperature varied about a nearly constant value for the remainder of each simulation. Analysis was conducted on averages of the final 20 years of each simulation.

4 Methane uptake in the simulated present-day climate

The characteristics of methane uptake in the present-day, model-simulated climate were examined first. A spatial map of the 20-year annual mean uptake is shown in Fig. 1a. As in Paper I, the regions of largest uptake are in South America, sub-Saharan and far southern Africa, and south-central Australia. As noted there, some of the highest uptake cells border large deserts, where spatial variability is high due to the low soil moisture threshold effect of r_{SM} (Sect. 4.2 of Paper I).

Figure 1a may be compared with the results of Paper I (Fig. 6a, on the same colour scale), in which CLASS was forced with reanalysis data from the 21-year (1979–1999) Global Land Surface Dataset (GOLD) of Dirmeyer and Tan (2001). This experiment will hereafter be referred to as the "GOLD" run. The difference between the two maps, after averaging the model map onto the coarser resolution of the GOLD run, is shown in Fig. 1b. Although the pattern of uptake is quite similar in the two cases, the global total of 24.8 Tg CH_4 y^{-1} derived from the GCM climate is 11% smaller than the 28.0 Tg CH_4 y^{-1} found under the reanalysis forcing. The most notable difference regionally is the generally larger uptake over South America in the GOLD run, although differences of comparable size and the same sign are also seen in eastern Russia, southern China/Himalayas and western North America. Conversely, the coupled model simulates notably larger uptake than in the GOLD run over sub-Saharan Africa, Mongolia, western Amazonia, and much of Australia. Relatively speaking, the discrepancy is largest at northern high latitudes, where at some grid points the uptake is over 80% larger under the reanalysis forcing, although it should be noted that CH_4 consumption is typically quite low in these regions to begin with.

Printer-friendly Version

Interactive Discussion

There are two principal causes of the positive anomalies seen in Fig. 1b. First, as shown in Fig. 2a, the top soil layer temperature in the GOLD run is generally larger (by +2.5°C, in the global mean) than in the coupled model simulation. The largest differences are seen in western North and South America, sub-Saharan Africa, and the western Himalayas. Comparison of the annual mean GOLD 2-m surface air temperature with ERA-40 data (not shown) over the same period (1979–1999) reveals a similarly distributed pattern of temperature bias in the GOLD reanalysis. The discrepancy is largest in arid and high elevation ($\gtrsim$2000 m) regions, where the temperature difference is of magnitude 4–20°C. Particularly notable is a 8–12°C bias over the western two-thirds of the Sahara; although most of the latter region is masked out of the uptake calculation (see auxiliary Fig. 1, Paper I), grid cells along the southern boundary are included. North of ~45°N, the GOLD and ERA-40 surface air temperatures are in better agreement, with the differences confined to the range –4 to +2°C. Since much of Asia and all of Australia have a negative temperature bias in GOLD, the global (land-only) average surface air temperature difference between the two datasets (GOLD minus ERA-40) is only +0.87°C.

One sees less of a difference between the ERA-40 and coupled model surface air temperatures (not shown), with the anomalies confined to the range ±2°C over most land areas, except in western North America and Asia north of ~45°N, where the ERA-40 values are systematically larger by 2–6°C at most locations. The global mean difference (ERA-40 minus model, land only) is +1.2°C. While the sum of these global mean differences (ERA-40 minus model plus GOLD minus ERA-40) is still smaller than the T_{soil} difference between the GOLD and coupled runs (+2.5°C), there is a good correspondence between the air and soil temperature difference patterns over all regions south of ~30°N. The larger magnitude of the soil temperature difference is consistent with the higher specific heat of soil, especially when moist, compared to air.
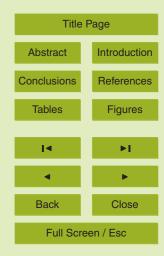
From the above results I infer the following. First, due to a high surface temperature bias (GOLD minus ERA-40) in the data used to drive the offline CH_4 uptake scheme, it is likely that CH_4 uptake in the extratropics was overestimated in Paper I. Second, due

to a low surface temperature bias (model minus ERA-40) in the northern extratropical land areas compared to observations, it is likely that CH_4 uptake in these regions is underestimated by the version of the coupled GCM used in this study. Thus, treating these biases as roughly equal but opposite in sign, I adopt a range of 24.8–28.0 Tg CH_4 y^{-1}

5 as a reasonable annual mean estimate for the present-day globally integrated CH_4 consumption. Including the uncertainty in the base oxidation rate constant k_0 as outlined in Paper I, this translates into a (2σ) range of J=8–47 Tg CH_4 y^{-1}. While the level of disagreement between the GOLD and ERA-40 air temperatures is disconcerting, and suggests replacing the former by the latter in future offline runs, it does not impact

10 the goal of the present study: namely, to simulate the difference between present and future climate (including air and soil temperatures), and CH_4 uptake derived from the latter, using the coupled model.

The temperature biases just described translate into differences in the methane uptake pattern seen in Fig. 1b in the following manner. While the larger T_{soil} of the GOLD

15 run enhances uptake in most of North and South America and much of Asia, it reduces J in sub-Saharan Africa. There, temperatures in the GOLD run frequently exceed 27.5°C, where r_T attains its maximum value, leading to extensive regions of negative r_T change (not shown). Central and southern Australia is another large area over which r_T decreases, but here a coincident decrease in T_{soil} is seen (Fig. 2a). More generally, it

20 is the more modest elevated soil temperatures (0 to +4°C) over the central continental regions in the GOLD run that are responsible for the bulk of the global methane uptake discrepancy due to differing soil temperatures.

A second contribution to the discrepancy in J comes from differences in the diffusion coefficient, D_{soil}, as shown in Fig. 2b. Since D_{soil} has only a weak temperature

25 dependence (Eq. 2), these differences are attributable to significantly different air-filled porosity, and thus fractional water content, θ, in the two simulations. The spatial pattern of the D_{soil} difference clearly mirrors that of J at high northern latitudes, where differences in J between the GOLD and coupled runs are largest in relative (but not absolute) terms. By contrast, T_{soil} is biased negative in the GOLD reanalysis over more

than half the land area at these latitudes, implying that the larger uptake in the offline calculation is not temperature-related. In these regions, the magnitude of the D_{soil} difference indicates that θ is approximately 50% smaller in the GOLD run.

The D_{soil} differences south of ~30° N are well-correlated with the annual mean precipitation difference between the two runs (not shown). Over much of South America, equatorial Africa, and Australia, the soil is drier in the model simulation than in the GOLD run, leading to a larger model D_{soil}. The model has slightly more precipitation than the reanalysis over most of the northern extratropics, and also less evaporation, consistent with the lower model D_{soil} there. The large relative differences seen in D_{soil} are, however, mostly due to differences in snow cover between the model and reanalysis data. Due to the low intrinsic diffusivities present at high latitudes, ~10^{-5} to a few $\times 10^{-3}$ cm^2 s^{-1}, even a small change in the surface water balance has a marked impact on diffusivity and, therefore, on methane uptake (see ff. Sect. 5.1.4). Comparison of Figs. 1b and 2b suggests that despite larger diffusivities in the coupled model in the tropics (where over two-thirds of the global annual uptake occurs in the GOLD run; Fig. 6a of Paper I), the discrepancy in CH$_4$ uptake is dominated by the soil temperature bias, since the mean J over the tropics remains larger in the GOLD-forced simulation.

5 Methane uptake in a simulated future climate

5.1 Annual mean results

In the simulated future climate, CH$_4$ consumption is expected to increase linearly with surface concentration C_{CH_4}, according to Eq. (1). Thus, in the absence of other changes, the globally uniform increase of C_{CH_4} from 1.720 ppmv to 1.974 ppmv under the SRES A1B concentration scenario (0.254 ppmv or 15%) would lead to an increase in global uptake of the same magnitude, i.e. an increase of 3.72 Tg CH$_4$ y^{-1} over the present day value of 24.8 Tg CH$_4$ y^{-1}. In fact, the globally integrated uptake in the future run is 30.4 Tg CH$_4$ y^{-1}, 23% higher than the present day value. Since this study

focuses on the effects of climate change on the character of CH_4 uptake, independent of the increase due to elevated concentration alone, the effect of the latter is removed in the analysis that follows, except when citing absolute uptake values in the future climate.

A spatial map of the 20-year annual mean difference in uptake between 2100 and present-day, with the concentration effect removed, is shown in Fig. 3. The relative change in uptake, $\Delta J/J=[J(2100)/J(1994)-1]\times100\%$ (Fig. 3b), is less than $\pm20\%$ over most of the Southern Hemisphere (SH) land areas and the Northern Hemisphere (NH) tropics (0–30° N), with the exception of the east coast of S. America from 15° S to 15° N, N. Africa, and western Mexico, where decreases of 20–50% are seen. With the exception of two adjacent grid cells in Somalia and Kenya (see ff. Sect. 5.1.3), large relative increases in J (>40%) are seen only in the NH extratropics, and exceed +120% in many areas, mostly in the Arctic. The global mean change of J, with the concentration effect removed, is +7.5%.

As alluded to in the Introduction, changes in the annual mean J are due to both increased surface heating in the future climate, which affects both sub-surface temperature and soil moisture (through evaporation), and to differences in future precipitation (rain and snow) patterns and amount, which affect D_{soil} (recall that the model land cover in 2100 remains unchanged from present-day). Figure 4a–c show the corresponding difference patterns for r_T, r_{SM} and D_{soil}. While certain similarities in patterns can be detected between Figs. 3 and 4, interannual variability of many of the fields can make attribution difficult. The contribution of the relative changes in ΔD_{soil}, Δr_T, and Δr_{SM} to ΔJ at each grid cell can be derived directly from Eq. (1):

$$\frac{\Delta J}{J} = \left(\frac{D^*_{soil}}{D_{soil}}\frac{r^*_T}{r_T}\frac{r^*_{SM}}{r_{SM}}\right)^{1/2} - 1 \tag{3}$$

$$\approx \frac{1}{2}\left(\frac{\Delta D_{soil}}{D_{soil}} + \frac{\Delta r_T}{r_T} + \frac{\Delta r_{SM}}{r_{SM}}\right), \tag{4}$$

where the superscript "*" indicates the value in 2100 (i.e., $D^*_{soil}=D_{soil}+\Delta D_{soil}$, ..., etc.)

and the second relation holds if all the Δ's are small compared to present day (a good approximation over 40°S–40°N). Hence, each of these agents contributes to $\Delta J/J$ in the same proportion; it remains only to assess the relative changes in the fields themselves over the region of interest. The zonally averaged results of this comparison are shown in Fig. 5. Note that due to the larger magnitude of the changes at high northern latitudes, a different vertical scale has been used for 40–75°N.

In order to better understand the space-time correlation between $\Delta J/J$ and each of the three predictor fields, as well as amongst the predictor fields themselves, a regression analysis was also performed using the individual monthly mean output from which the 20-year mean fields were constructed. The Pearson (linear) correlation coefficient r was calculated from 240 individual monthly grids of each relative difference field (i.e., $\Delta J/J$ versus $\Delta D_{soil}/D_{soil}$, $\Delta J/J$ versus $\Delta r_T/r_T$, ..., etc.), over separate bands of latitude as presented in Table 1. The magnitude of r reflects the degree to which the change in some quantity is correlated ($r>0$) or anti-correlated ($r<0$) with another quantity over that range in latitude. Figure 5 and Table 1 should be referred to as the role of each of these contributors is considered in turn.

5.1.1 Soil temperature

The mean increase in T_{soil} from the present to 2100 is 3.5±1.4 °C, and the geographical pattern (not shown) resembles previously published results, particularly with respect to the marked warming asymmetry at northern high latitudes (Hegerl et al., 2007). This ΔT_{soil} leads to changes in the factor r_T that generally resemble ΔT_{soil}, except in the tropics where $\Delta r_T<0$, as shown in Fig. 4a. There, temperatures frequently exceed 27.5°C, where r_T attains its maximum value, leading to extensive regions of negative Δr_T in South America, sub-Saharan Africa, and northern Australia. The contribution of $\Delta r_T/r_T$ to $\Delta J/J$ ranks second to that of diffusivity at most latitudes, although it exceeds $\Delta D_{soil}/D_{soil}$ between 20–40° S and 35–55° N (Fig. 5 and Table 1). In general, $\Delta r_T/r_T$ and $\Delta D_{soil}/D_{soil}$ are weakly correlated, with the closest correspondence in the mid-latitudes, where increases in T_{soil} lead to soil drying and higher air-filled porosity

Future consumption of methane by soil

C. L. Curry

and diffusivity. $\Delta r_T/r_T$ and $\Delta r_{SM}/r_{SM}$ are anti-correlated over southern mid-latitudes, indicating increased moisture stress under warming, but are only weakly correlated elsewhere, since r_{SM} depends more directly upon soil water content, and thus diffusivity, than T_{soil} (see Sect. 5.1.3).

5.1.2 Precipitation, evaporation, and soil moisture

According to the Clausius-Clapeyron relation, higher specific humidity in a warmer atmosphere should lead to increased poleward moisture transport and hence increased precipitation at high latitudes. This increase is seen in our simulations nearly everywhere north of 45°C in the future climate, with a more mixed difference pattern in the tropics and subtropics (not shown). The global, land-only, precipitation change in future is $\Delta P = +56\,\mathrm{mm\,y^{-1}}$ (+6%). Increases in evaporation are seen on every continent, and while these are generally of smaller magnitude than the precipitation changes ($\Delta E = +39\,\mathrm{mm\,y^{-1}}$) – i.e., $\Delta(P-E)$ is positive – globally $\Delta E/E$ exceeds $\Delta P/P$ by ~1%. In the global mean, the net effect of these atmospheric moisture changes on the upper layer soil moisture θ_w is not significant; i.e., $\Delta\theta_w = -3.6 \times 10^{-3}$. However, the regional variation of $\Delta\theta_w$ (roughly complementary to that of D_{soil}; see Fig. 4c) has an important influence on two of the principal determinants of the CH_4 soil uptake: namely, the soil moisture stress factor r_{SM} and the diffusivity D_{soil}.

5.1.3 Soil moisture stress

As shown in Fig. 4b, r_{SM} increases nearly everywhere north of 45°C in the future climate, except in western Europe (where $P-E$ decreases) and western North America (where $P-E$ increases but runoff to the Pacific Ocean is large). The strongest increases are seen over western Asia and the Great Plains of North America, where present day values of r_{SM} are well below the global mean. Even a modest increase in soil water content over these areas, as seen in Fig. 4b, can lead to a large relative increase in r_{SM}. Indeed, even in regions where the annual mean soil moisture θ_w

Title Page

Abstract | Introduction

Conclusions | References

Tables | Figures

|◄ | ►|

◄ | ►

Back | Close

Full Screen / Esc

Printer-friendly Version

Interactive Discussion

decreases in future (such as eastern Europe), r_{SM} can still increase, as long as θ_w increases in the drier months. This is due to the insensitivity of r_{SM} to θ_w at large θ_w (Eqs. 8 and 9 in Paper I). In this regime, methane uptake is limited by diffusivity, not r_{SM}, and hence the pattern of r_{SM} more closely resembles that of P, not θ_w. Thus, despite the strong and widespread increase seen in Fig. 4b, the correlation of r_{SM} with J is generally weak at northern latitudes. This is due to similarly distributed decreases in D_{soil} (see below), which limit the overall J increase.

Substantial decreases in r_{SM} are seen south of $\sim$30° N, with the largest regional decreases (20–60%) seen on the east coast of S. America from 15° S to 15° N, N. Africa and the Middle East, and western Mexico. These are also areas of strongly decreased methane consumption in future (Fig. 3). Positive correlations of Δr_{SM} with ΔJ are seen at latitudes south of $\sim$ 30° N (Table 1), suggesting that decreased water availability is largely responsible for the reduced or weakly enhanced methane uptake in these regions. Two-dimensional correlation maps (not shown) show that only in Amazonia is the influence of temperature ($\Delta r_T < 0$) comparable to that of r_{SM} in this respect. Notable exceptions to the decreasing r_{SM} trend south of $\sim$ 30° N are equatorial eastern Africa and northern Australia, where large increases in annual precipitation lead to a partial alleviation of moisture stress in those regions (Fig. 4b). In locations where r_{SM} is particularly low in the present climate (e.g., at the two adjacent grid cells in Somalia and Kenya previously noted in Sect. 5.1), large relative increases in r_{SM} and, consequently, J occur.

Generally speaking, decreasing precipitation in future in the tropics leads to decreased soil water, which lowers r_{SM}. Where decreases in the latter are largest, methane uptake decreases. However, the land area where $\Delta J < 0$ is smaller than that of $\Delta r_{SM} < 0$, due to the competing influences of temperature and diffusivity. Table 1 shows that Δr_{SM} and ΔD_{soil} are strongly anti-correlated at nearly all latitudes, with the tightest relation holding between 60° S and 30° N. This reflects the dominant dependence of both factors on θ_w. As seen in Fig. 5, soil temperature and diffusivity are the dominant controls on methane uptake at high latitudes, and even substantial changes

Future consumption of methane by soil

C. L. Curry

in r_{SM} have little impact.

5.1.4 Diffusivity and snow cover

The pattern of future diffusivity change, shown in Fig. 4c, is the complement of the change in soil moisture, θ_w, mentioned above. D_{soil} increases more or less uni-
formly across Europe, the United States, and South America, with more heterogeneous changes seen elsewhere. The global and annual mean change in D_{soil} is +5.1%, de-spite the fact that $\Delta(P-E)>0$, implying that soil moisture vertical transport and storage play an important role. In particular, the positive sign of ΔD_{soil} cannot be taken as sim-ply an indication of increased evaporation in a warmer climate, independent of other
factors. Figure 5 and Table 1 show that ΔD_{soil} and ΔJ are anti-correlated in the equa-torial band, coincident with positively correlated Δr_{SM}, due to the anomalous drying of the soil in these regions (and, in the case of the Amazon, a significant decrease in r_T). The strongest positive correlations of ΔD_{soil} with ΔJ are seen north of 60° N ($r=0.69$).

It is apparent from Fig. 4c that ΔD_{soil} is highly spatially variable in east Asia, where
the relative change in J is also the largest anywhere on the globe (Fig. 3b). This characteristic is likely linked to changes in future snow cover at those locations. As Fig. 4d shows, the snow cover difference pattern over east Asia (and far northern Canada, another region with strongly-varying D_{soil}) is also highly spatially variable with alternating sign, in contrast to other NH locations. The marked east-west asymmetry
in snow cover change over northern Asia is the result of a similarly asymmetric pattern of snowfall change. Positive D_{soil} changes are associated with areas of decreasing snow cover, albeit of smaller magnitude. However, due to the aforementioned low soil diffusivities at high latitudes (Sect. 4), even small changes in surface water balance can strongly affect diffusivity. Moreover, soil porosities in east Asia are ∼15–25% smaller
than in west Asia and Europe (Zobler, 1986), meaning that increased soil water from spring snow melt in east Asia more strongly moderates diffusivity and uptake there. In Europe and western Asia, less snow above ground in winter leads to decreased soil moisture in NH summer, and thus to higher annual mean D_{soil}.

Hence, I conclude that while the presumption of increasing diffusivity under surface warming holds for global and even zonal means, it fails over large geographic areas where less porous soils underlie a more varied hydrological regime. Further, while areas of strong increase in D_{soil} lead to similarly large increases in J, beneficial changes in r_T and r_{SM} lead to positive ΔJ even where D_{soil} decreases. Thus the pattern of ΔJ is considerably smoother than that of ΔD_{soil}, as seen in Fig. 4.

To sum up the annual mean results, Fig. 4a, b and c taken together give an accurate picture of how the relative change in each of the key factors contributes to the change in methane flux at individual grid locations. The zonal means of these fields, shown in Fig. 5, allow a more direct comparison of the relative strengths of these factors at different latitude, while Table 1 shows the corresponding correlation coefficients. Finally, note that due to spatial and temporal averaging, large regional correlations and anti-correlations can sometimes sum to near-zero mean values. This explains why, e.g., ΔJ and ΔD_{soil} are essentially uncorrelated in the zonally averaged 30–60° S latitude band (Table 1), despite the large relative contribution of ΔD_{soil} to ΔJ evident in Fig. 5.

5.2 Seasonal differences

I now investigate how future methane uptake changes depend on latitude and season. Figure 6 is a Hovmueller diagram showing the seasonality of various zonally averaged fields, each normalized by the fractional land area at each latitude. The seasonal cycle of methane uptake in the present day climate is shown in Fig. 6a. The continuous band of high uptake at ∼15° N corresponds to the sub-Saharan maximum seen in Fig. 1a, which dominates the small land area at that latitude. Three distinct maxima in uptake from May–September are evident in the northern extratropics, due to favourably low diffusivity in NH summer. The largest zonal mean uptake occurs over 10–15°S from January to May, when sufficient moisture is available and r_{SM} is close to unity over most of sub-equatorial South America and Africa. This situation changes dramatically in May, when r_{SM} falls to <0.4 in these areas, and remains low until October.

Figure 6b shows the difference between zonally averaged uptake in the present and future climates. To better understand how ΔD_{soil}, Δr_T, and Δr_{SM} contribute to the pattern of ΔJ, I also show Hovmueller plots of these quantities in Fig. 6c, d, and e. Uptake increases at mid- to high northern latitudes year round, with a maximum of +108 mg CH$_4$ m^{-2} y^{-1} (a 68% increase over present day values) in June. Inspection of 2-D maps of monthly ΔJ show the largest absolute increases of over 600 mg CH$_4$ m^{-2}y^{-1} occur in western and north-central Russia in June, and in western Brazil in September. Comparing Fig. 6a and 6b shows that the largest increases in uptake generally occur at or near uptake minima in the present day state. For example, in the present state at 50° N, CH$_4$ consumption essentially ceases between January and March each year as T_{soil} falls below freezing. In the future climate, however, J exceeds 40 mg CH$_4$ m^{-2} y^{-1} in all months at this latitude. The largest relative change in NH methane uptake occurs from October to April at 70–80°N, when consumption can increase by a factor of ten or more over the small present day values (Fig. 6a).

The results of Table 1, Figs. 5 and 6 imply that the uptake enhancement at high northern latitudes is due to the joint increase of r_T and D_{soil} into the future period. Specifically, the poleward extension of warmer temperatures is chiefly responsible for the year-round increase in methane flux in 2100, while the summer peak in ΔJ can be ascribed to a corresponding increase in D_{soil}, the result of increased evaporation in summer. Although r_{SM} also displays a large increase north of 40° N from fall through spring (Fig. 6e), this is largely countered by decreases in D_{soil} due to higher snowmelt, leading to a weak correlation between Δr_{SM} and ΔJ at these more northerly latitudes (Table 1).

In the SH, a notable increase in J occurs between mid-July and September (Fig. 6b). From mid-September until the end of the year, large increases in uptake are seen in all SH land areas poleward of 25°S. In southern Chile, as in the NH, uptake enhancement is due to the poleward shift of the soil temperature isotherms – but this is virtually the only SH location where it occurs. As can be seen from Fig. 6b to e, the CH$_4$ flux increase in SH spring-summer is much better correlated with increases in r_{SM} than in

either r_T or D_{soil}; indeed, D_{soil} shows a strong anti-correlation in this instance. The tendency for J to decrease with decreasing r_{SM} is also seen quite clearly in Figs. 6b and e. This emphasizes once again the prevailing influence of r_{SM} in the SH, paralleling that of r_T in the NH. In general, the pattern of ΔD_{soil}, which largely complements that of Δr_{SM} (as expected, since increasing soil moisture leads to decreased air-filled porosity), appears to be of secondary importance. One exception is from May–September at 30–40°S, where a persistent decrease in D_{soil} causes $\Delta J < 0$, even in the presence of increased r_{SM}. But aside from this, D_{soil} has a discernable effect on ΔJ only when reinforced by an associated change in r_T. An example of this occurs in January–February at 50°S (southern Chile, where the largest ΔD_{soil} occurs globally), where a large decrease in D_{soil} coupled with a slight decrease in r_T leads to a local minimum in ΔJ.

5.3 Change in uptake by ecosystem type

Analysis of the geographical distribution of methane consumption under meteorological forcing in Paper I revealed that subtropical and dry tropical ecosystems account for over half of the present-day uptake. I now examine how the distribution of uptake over ecosystem type (as represented by aggregated Holdridge life zone; see Paper I) is altered by climate change, assuming a static distribution of ecosystem types. While the latter supposition is likely invalid under strong climate forcing, this approach does permit a straightforward accounting of changes to uptake in specific geographical regions.

Table 2 shows that, with the exception of tropical and subtropical deserts, where ΔJ is considerably lower than the values seen elsewhere, the change in areal uptake lies in the narrow range of 42–55 mg CH_4 m^{-2} y^{-1} across ecosystem types. However, the relative increase in uptake is up to three times larger in polar, boreal and cool temperate regions than in the subtropics and tropics. This is consistent with the results of Sect. 5.1 and Fig. 3b in particular, which shows large relative increases in flux only in the NH extratropics. Subtropical forests, which had the largest areal and total CH_4 consumption in Paper I, also undergo the largest total increase in future. But the largest

Future consumption of methane by soil

C. L. Curry

areal increase occurs in boreal forest ecosystems, resulting in a total uptake change that is almost as large as for subtropical forests.

6   Discussion and conclusions

R99 approximated the effect of climate change upon methane uptake in their offline model by calculating the total CH_4 uptake under a globally uniform T_{soil} increase. When the authors fixed the model soil moisture at present-day values, they found that following a small increase from $\Delta T_{soil}=0$ to $1.5°$, J decreased at higher ΔT_{soil} due to the frequent exceedence of the r_T maximum in the tropics (Sect. 5.1.1). This led R99 to conclude that the effect of temperature increase alone (of magnitude $\gtrsim 1.5°$) is to decrease total methane uptake. In a second calculation, R99 allowed the soil moisture (but not precipitation) to vary according to their hydrological model response to ΔT_{soil}. In this case, decreasing soil moisture from rising temperatures and higher evaporation rates increased diffusivity overall, causing J to increase by 9% globally at $\Delta T_{soil}=5°C$. The role of r_{SM} in this experiment is not clear; presuming it was allowed to vary with soil moisture, this means that J would have increased further had $r_{SM}=1$. However, the neglect of precipitation changes in the second experiment probably overestimated D_{soil} in the extratropics, likely leading to an overestimated ΔJ there (e.g., see Fig. 5).

In the present study, a more complex interplay of the influence of temperature, soil moisture, and moisture stress on methane uptake has emerged. The model develops a non-uniform pattern of both soil temperature and precipitation change from present-day to 2100, which results in the complex pattern of ΔJ displayed in Fig. 3. Remarkably, however, the global mean value of $\Delta J=+7.5\%$ agrees closely with R99's second estimate, especially when the lower global mean $\Delta T_{soil} = 3.5°$is considered (the corresponding R99 value at the same ΔT_{soil} is +7.6%). But as Fig. 5 shows, R99's assessment of the role of the sensitivity of J to separate changes in T_{soil} and D_{soil} is too simplistic.

In our experiments, the increase of T_{soil} in the tropics does lead to lower r_T, and

thus decreased J over the range 10° S–15° N, but the change is much smaller than the increases seen at higher latitudes (Fig. 5). The small tropical Δr_T is likely due to the combined effect of lower than average $\Delta T_{soil} \simeq 3.0°$C and decreasing precipitation over land at these latitudes. By neglecting ΔD_{soil} and Δr_{SM} in Eq. (3), one can approxi-
5 mate the effect of fixed soil moisture on our results. The resulting global mean relative change in J due to Δr_T alone is ~+2%, or more than one-quarter of the total change in J, not a decrease in J as predicted by R99.

It is also apparent from our results that, even when diffusivity decreases, J can increase due to increased soil temperature and favourable r_{SM} in the extratropics (e.g.,
10 over eastern Asia in Fig. 4). The annual mean diffusivity increases over ~60% of land-only grid cells north of 45° N, while J increases over 98% of the cells and T_{soil} increases globally. As discussed in Sect. 5.1.4, diffusivity is strongly controlled by factors other than temperature, including precipitation, porosity, and snow cover (Sect. 5.1 and Fig. 4d and e).

15 Using the same model configuration, I also investigated the behaviour of the soil methane sink under differing surface GHG concentration forcings, specifically for pre-industrial and other future concentration scenarios. Table 3 compares the global mean uptake results for the A1B scenario in 2100 with the A2 and B1 scenarios, and also with a simulation using preindustrial (circa 1850) GHG concentrations. Recall that most of
20 the variation in J between scenarios (column 2 of Table 3) arises from differences in CH_4 concentration at various epochs. For example, the preindustrial and A2 scenario CH_4 concentrations differ by a factor of 4.7, while the ratio of their respective J values is 5.5. To gauge the effect of climate change alone on CH_4 consumption, column 3 of Table 3 shows ΔJ with the concentration effect removed. The global mean uptake
25 change based on the future scenarios ranges from +4 to 11%. As might be expected, the global mean ΔJ scales roughly with the corresponding temperature change, with $\Delta J < 0$ in the preindustrial simulation. The preindustrial uptake is 5% below the present day value. The most scenario-dependent of the primary factors appears to be Δr_T, except in the A2 scenario, where the relative increase in ΔD_{soil} is larger, possibly due

Future consumption of methane by soil

C. L. Curry

Title Page

Abstract | Introduction

Conclusions | References

Tables | Figures

|◄ | ►|

◄ | ►

Back | Close

Full Screen / Esc

Printer-friendly Version

Interactive Discussion

to larger evaporation at high latitudes than in the other scenarios.

Interestingly, the global mean change in the soil moisture stress factor r_{SM} is small and of positive sign in all scenarios and, moreover, is relatively insensitive to scenario. This is somewhat surprising, given that r_{SM} was found to be the chief factor limiting uptake in Paper I. This outcome is the result of offsetting changes north and south of ~45° N in all of the simulations (Fig. 4b; note that land north of 45° N comprises 36% of the global land area, omitting Greenland and Antarctica). Many qualitative predictions of soil water availability in a warmer climate seem to have overlooked the possibility of increasing r_{SM} at high northern latitudes due to increased snowmelt and/or snowfall, as seen in the simulations presented here. Even in the A2 scenario, where the annual mean surface air temperature change north of 45°N is 7.1°C by 2100, r_{SM} still increases by 4.4%.

While this work is a first attempt at calculating the change in methane uptake at the global scale, the influence of several factors has been neglected. Among these are: 1) anthropogenic land-use change, which leads to changes in the cultivation fraction r_N with time (Ojima et al., 1993); 2) the evolution of natural wetlands, which leads to a changing pattern of r_W; 3) changes in the spatial distribution of ecosystem types, which requires a dynamic vegetation model; and 4) the incomplete characterization of soils, due to the use of a single, global soil texture dataset, and the effect of changes in soil type and physical characteristics at centennial time scales, which no prescribed dataset can capture.

However, the most evident limitation of the present approach is its neglect of methanogenesis, as the method applies only to unsaturated surface soils where aerobic processes dominate over anaerobic ones. Although wetlands cover only around 5% of the Earth's ice-free land surface (Prigent et al., 2009), they are responsible for a disproportionate fraction of global methane emissions (25–40% of the annual total, according to a range of estimates; Denman et al., 2007), and thus need to be included in any dynamic model of the methane budget. A more complex soil thermal and hydrological scheme than that used here, including a dynamic water table, is needed

Future consumption of methane by soil

C. L. Curry

Printer-friendly Version

Interactive Discussion

Future consumption of methane by soil

C. L. Curry

ı◄ | ►ı

◄ | ►

Back | Close

Full Screen / Esc

Printer-friendly Version

Interactive Discussion

to capture the behaviour of key biogeochemical feedbacks, such as methane release to the atmosphere by northern wetlands and carbon sequestration in peatlands under future warming. Progress is now being made in this direction by other researchers (Zhuang et al., 2004; Wania et al., 2009).

Another shortcoming of the present calculations, which is readily remedied, is the adoption of a single uniform value for the CH_4 surface concentration. Current observations indicate a significant north-south gradient in surface CH_4, of order 140 ppbv or 8% of the global mean value (Climate Monitoring and Diagnostics Laboratory). Since both CH_4 concentrations and land area are largest in the NH, using a more realistic surface concentration distribution should lead to an even larger north/south imbalance in the methane sink than already seen (approximately 60/40, according to Paper I), and a slightly larger global uptake. Furthermore, the parameterization of methane consumption utilized in this paper can be combined with a simplified atmospheric CH_4 chemistry scheme, already tested in AGCM3 (Curry et al., 2006), to enable completely prognostic methane sinks in a coupled GCM. For a prescribed surface CH_4 concentration field, running the model to equilibrium would then determine the relative contributions of the atmosphere and soil to the total CH_4 sink. Alternatively, if instead the surface source distribution of CH_4 emissions (∼60% of which are anthropogenic) were prescribed, this would allow the determination of the 3-D methane concentration field. The latter approach would then be suitable for use in transient climate simulations, e.g., along the lines of the C^4MIP-type experiments conducted with carbon cycle GCMs (Friedlingstein et al., 2006).

In the meantime, the estimates of the present paper give some notion of what to expect on the methane consumption side of the ledger in future decades. In particular, this work has clearly identified the relative roles of the key contributing factors to methane consumption in the majority of climatic zones and biomes.

Sciences, as part of the Canadian Global Coupled Carbon Climate Model (CGC^{3}M) research network.

References

Climate Monitoring and Diagnostics Laboratory: GLOBALVIEW—CH$_4$: Cooperative Atmospheric Data Integration Project—Methane, CD-ROM, NOAA, Boulder, Colo., also available via anonymous ftp at ftp.cmdl.noaa.gov, path ccg/ch4/GLOBALVIEW, 2001. 6098

Curry, C. L.: Modelling the soil consumption of atmospheric methane at the global scale, 21, GB4012, doi:10.1029/2006GB002818, 2007. 6078, 6079

Curry, C. L., McFarlane, N. A., and Scinocca, J. F.: Relaxing the well-mixed greenhouse gas approximation in climate simulations: Consequences for stratospheric climate, J. Geophys. Res., 111, D08104, doi:10.1029/2005JD006670, 2006. 6098

Denman, K. L., Brasseur, G., Chidthaisong, A., Ciais, P., Cox, P. M., Dickinson, R., Hauglustaine, D., Heinze, C., Holland, E., Jacob, D., Lohmann, U., Ramachandran, S., da Silva Dias, P., Wofsy, S. C., and Zhang, X.: Couplings Between Changes in the Climate System and Biogeochemistry, in: Climate Change 2007: The Physical Science Basis. Contribution of Working Group I to the Fourth Assessment Report of the Intergovernmental Panel on Climate Change, edited by: Solomon, S., Qin, D., Manning, M., Chen, Z., Marquis, M., Averyt, K. B., Tignor, M., and Miller, H. L., 499–587, Cambridge Univ. Press, Cambridge and New York, 2007. 6078, 6097

Dirmeyer, P. and Tan, L.: A multi-decadal global land-surface data set of state variables and fluxes, COLA Tech. Rep. 102, Centre for Ocean-Land-Atmosphere Studies, Cent. for Ocean-Land-Atmos. Stud., Calverton, Md., also available at http://www.iges.org/pubs/tech.html, 2001. 6083

Dutaur, L. and Verchot, L. V.: A Global Inventory of the Soil CH$_4$ Sink, 21, GB4012, doi:10.1029/2006GB002818, 2007. 6079

Friedlingstein, P., Cox, P., Betts, R., Bopp, L., von Bloh, W., Brovkin, V., Cadule, P., Doney, S., Eby, M., Fung, I., Bala, G., John, J., Jones, C., Joos, F., Kato, T., Kawamiya, M., Knorr, W., Lindsay, K., Matthews, H. D., Raddatz, T., Rayner, P., Reick, C., Roeckner, E., Schnitzler, K.-G., Schnur, R., Strassmann, K., Weaver, A. J., Yoshikawa, C., and Zeng, N.: Climate-

carbon cycle feedback analysis: Results from the C^4MIP model intercomparison, J. Climate, 19, 3337–3353, 2006. 6098

Hanson, R. S. and Hanson, T. E.: Methanotrophic bacteria, Microbiol. Rev., 60, 439–471, 1996. 6079

5 Hegerl, G. C., Zwiers, F. W., Braconnot, P., Gillett, N. P., Luo, Y., Orsini, J. A. M., Nicholls, N., Penner, J. E., and Stott, P. A.: Understanding and Attributing Climate Change, in: Climate Change 2007: The Physical Science Basis. Contribution of Working Group I to the Fourth Assessment Report of the Intergovernmental Panel on Climate Change, edited by: Solomon, S., Qin, D., Manning, M., Chen, Z., Marquis, M., Averyt, K. B., Tignor, M., and Miller, H. L.,
10 663–745, Cambridge Univ. Press, Cambridge and New York, 2007. 6088

Horz, H. P., Rich, V., Avrahami, S., and Bohannan, B. J. M.: Methane-oxidizing bacteria in a California upland grassland soil: Diversity and response to simulated global change, Appl. Environ. Microbiol., 71, 2642–2652, doi:10.1128/AEM.71.5.2642-2652.2005, 2005. 6079, 6080

15 Knief, C., Lipski, A., and Dunfield, P.: Diversity and activity of methanotrophic bacteria in different upland soils, Appl. Environ. Microbiol., 69, 6703–6714, doi:10.1128/AEM.69.11. 6703-6714.2003, 2003. 6079

McFarlane, N. A., Boer, G. J., Blanchet, J.-P., and Lazare, M.: The Canadian Climate Centre second-generation general circulation model and its equilibrium climate, J. Climate, 5, 1013–
20 1044, 1992. 6081

McFarlane, N. A., Scinocca, J. F., Lazare, M., and Harvey, R., Verseghy, D., and Li, J.: The CCCma third generation atmospheric general circulation model, 40 pp., CCCma Internal Rep., available online at http://www.cccma.ec.gc.ca/models/gcm3.shtml, 2005 6082

Ojima, D. S., Valentine, D. W., Mosier, A. R., Parton, W. J., and Schimel, D. S.: Effect of land
25 use change on methane oxidation in temperate forest and grassland soils, Chemosphere, 26, 675–685, 1993. 6097

Prigent, C., Papa, F., Aires, F., Rossow, W. B., and Matthews, E.: Global inundation dynamics inferred from multiple satellite observations, 1993–2000, J. Geophys. Res., 112, D12107, doi:10.1029/2006JD007847, 2009. 6097

30 Ridgwell, A., Marshall, S. J., and Gregson, K.: Consumption of atmospheric methane by soils: a process-based model, 13, 59–70, 1999. 6079

Roslev, P., Iversen, N., and Henriksen, K.: Oxidation and assimilation of atmospheric methane by soil methane oxidizers, Appl. Environ. Microbiol., 63, 874–880, 1997. 6079

Printer-friendly Version

Interactive Discussion

Schnell, S. and King, G. M.: Responses of methanotrophic activity in soils and cultures to water stress, Appl. Environ. Microbiol., 62, 3203–3209, 1996. 6080

Torn, M. S. and Harte, J.: Methane consumption by montane soils: implications for positive and negative feedback with climatic change, Biogeochemistry, 32, 53–67, 1996. 6080

Verseghy, D. L.: CLASS–A Canadian Land Surface Scheme for GCMs. I. Soil model, Int. J. Climatol., 11, 111–133, 1991. 6082

Verseghy, D. L.: Local climates simulated by two generations of Canadian GCM land surface schemes, Atmos. Ocean, 34, 435–456, 1996. 6082

von Fischer, J. C., Butters, G., Duchateau, P. C., Thelwell, R. J., and Siller, R.: In situ measures of methanotroph activity in upland soils: A reaction-diffusion model and field observation of water stress, J. Geophys. Res., 114, G01015, doi:10.1029/2008JG000731, 2009. 6081

Wania, R., Ross, I., and Prentice, I. C.: Integrating peatlands and permafrost into a dynamic global vegetation model: I. Evaluation and sensitivity of physical land surface processes, doi:10.1029/2008GB003412, in press, 2009. 6098

Zhuang, Q., Melillo, J. M., Kicklighter, D. W., Prinn, R. G., McGuire, A. D., Steudler, P. A., Felzer, B. S., and Hu, S.: Methane fluxes between terrestrial ecosystems and the atmosphere at northern high latitudes during the past century: A retrospective analysis with a process-based biogeochemistry model, 18, GB3010, doi:10.1029/2004GB002239, 2004. 6098

Zobler, L.: A world soil file for climate modelling, NASA Tech. Mem. 87802, NASA, 1986. 6091

Table 1. Linear (Pearson) correlation coefficients of indicated monthly mean fields.

	ΔD_{soil}	Δr_T	Δr_{SM}
60–90° N			
ΔJ	0.686	0.392	−0.076
ΔD_{soil}		0.152	−0.332
Δr_T			0.127
30–60° N			
ΔJ	0.144	0.161	0.175
ΔD_{soil}		0.205	−0.646
Δr_T			−0.107
0–30° N			
ΔJ	−0.122	0.215	0.355
ΔD_{soil}		−0.146	−0.911
Δr_T			0.142
30–0° S			
ΔJ	−0.207	0.207	0.408
ΔD_{soil}		−0.099	−0.932
Δr_T			0.094
60–30° S			
ΔJ	0.042	−0.028	0.226
ΔD_{soil}		0.240	−0.916
Δr_T			−0.293
Global			
ΔJ	0.514	0.201	0.250
ΔD_{soil}		0.043	−0.755
Δr_T			0.020

Future consumption of methane by soil

C. L. Curry

Table 2. Annual mean values at present-day and change (year 2100 minus present) in methane consumption by aggregated Holdridge life zone.

Class/Description	Area $10^6 \, km^2$	Areal Uptake, present-day $mg \, CH_4 \, m^{-2} \, y^{-1}$	Total Uptake, present-day $Tg \, CH_4 \, y^{-1}$	Areal Uptake Change, 2100[a] – present $mg \, CH_4 \, m^{-2} \, y^{-1}$	Total Uptake Change, 2100[a] – present $Tg \, CH_4 \, y^{-1}$ (%)
1 Polar/mountain desert	3.9	109.2	0.43	50.9	0.20 (47)
2 Tundra	10.1	85.1	0.86	41.8	0.42 (49)
3 Boreal desert/scrub	1.8	138.6	0.24	50.1	0.088 (36)
4 Boreal forest	16.1	135.5	2.18	54.5	0.88 (40)
5 Cool temperate desert/scrub	11.3	136.6	1.55	45.9	0.52 (34)
6 Cool temperate forest	11.2	143.8	1.61	44.1	0.50 (31)
7 Warm temperate desert/scrub	4.6	231.7	1.06	47.0	0.22 (20)
8 Warm temperate forest	5.3	253.5	1.34	53.7	0.29 (22)
9 Subtropical desert/scrub	17.3	179.7	3.11	32.0	0.55 (18)
10 Subtropical forest	26.3	273.4	7.18	43.1	1.13 (16)
11 Tropical desert/scrub	7.2	140.3	1.02	20.7	0.15 (15)
12 Tropical dry forest	10.8	274.3	2.97	41.8	0.45 (15)
13 Tropical moist forest	4.5	274.3	1.24	41.6	0.19 (15)
	Total	Mean	Total	Mean	Total
	130.5	190.1	24.8	42.8	5.58 (23)

[a] With concentration effect included (Sect. 5.1).

Table 3. Annual, global mean CH_4 uptake and change (difference from present day) in various quantities under specified forcing scenarios.

Scenario, epoch	J [a]	ΔJ [b]	ΔD_{soil}	Δr_T	Δr_{SM}
	$Tg\,CH_4\,a^{-1}$	%	%	%	%
Present, 1994 [c]	**24.8**	. . .	. . .	. . .	. . .
Pre−ind., 1850 [d]	10.2	−4.8	−2.8	−6.6	−1.5
B1, 2100 [e]	23.7	+4.4	+2.0	+3.7	+1.9
A1B, 2100 [f]	**30.4**	**+7.5**	**+5.1**	**+6.4**	**+3.0**
A2, 2100 [g]	56.6	+11.3	+10.0	+7.5	+4.4

[a] With concentration effect included (Sect. 5.1).

[b] With concentration effect removed (Sect. 5.1).

[c] Using concentrations CH_4=1720 ppbv, CO_2=358 ppm, N_2O=311 ppbv, CFC-11=266 pptv, CFC-12=522 pptv.

[d] Using historical (circa 1850) concentrations of CH_4=792 ppbv, CO_2=288 ppm, N_2O=275.5 ppbv, CFC-11=CFC-12=0.

[e] Using concentrations CH_4=1569 ppbv, CO_2=540 ppm, N_2O=375 ppbv, CFC-11=45 pptv, CFC-12=222 pptv.

[f] Scenario discussed in detail in Sect. 5 and 6, using concentrations CH_4=1974 ppbv, CO_2=717 ppm, N_2O=372 ppbv, CFC-11=45 pptv, CFC-12=222 pptv.

[g] Using concentrations CH_4=3731 ppbv, CO_2=836 ppm, N_2O=447 ppbv, CFC-11=45 pptv, CFC-12=222 pptv.

Fig. 1. (a) Global distribution of 20-year annual mean CH_4 uptake. Units are mg CH_4 m^{-2} y^{-1}. The globally integrated uptake is 24.8 Tg CH_4 a^{-1}. **(b)** Difference of 21-year annual mean CH_4 uptake with GOLD forcing minus 20-year annual mean CH_4 uptake from the model.
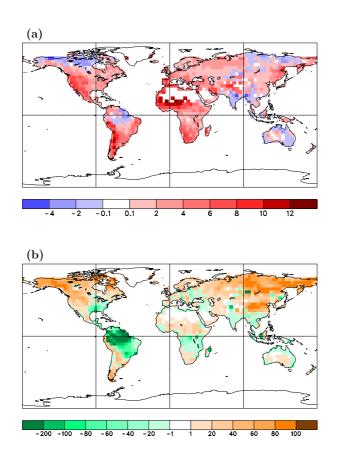
Fig. 2. Difference (GOLD minus coupled model) of 20-year annual mean: **(a)** top layer soil temperature, T_{soil}, in degrees; **(b)** diffusivity, D_{soil}, in percent.
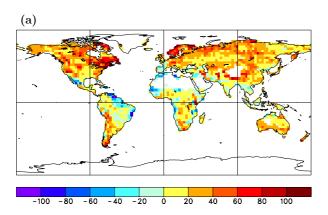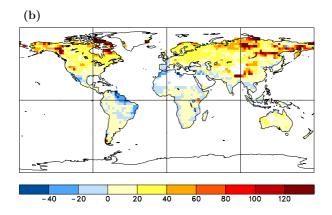
Fig. 3. Difference (2100 minus present-day) of 20-year annual mean CH_4 uptake, with the effect of the uniform concentration increase removed: **(a)** absolute values in mg CH_4 m^{-2} y^{-1}; **(b)** expressed as a percent.

Printer-friendly Version

Interactive Discussion

Fig. 4. Relative change (2100 minus present-day, in percent) of 20-year annual mean fields: **(a)** r_T; **(b)** r_{SM}; **(c)** D_{soil}; **(d)** snow cover.
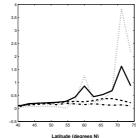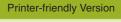
Fig. 5. Relative change (2100 minus present day) of the indicated 20-year annual mean fields as a function of latitude. Note that due to the larger magnitude of the changes at high northern latitudes, a different vertical scale is used for 40–75° N.
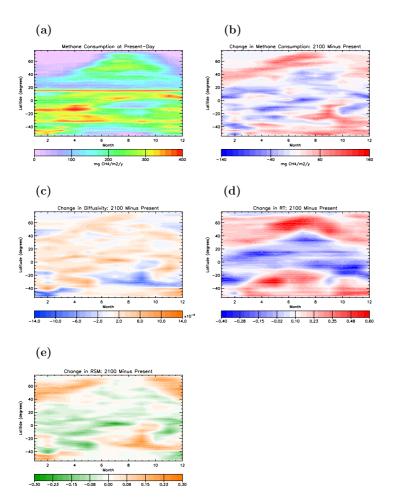
Future consumption of methane by soil

C. L. Curry

Fig. 6. Hovmueller diagram showing the seasonal cycle of **(a)** methane uptake in the present-day model climate (mg CH$_4$ m^{-2} y^{-1}), and differences between year 2100 and present-day of: **(b)** methane uptake (mg CH$_4$ m^{-2} y^{-1}); **(c)** diffusivity (cm^2 s^{-1}); **(d)** r_T (dimensionless); and **(e)** r_{SM} (dimensionless).